Energy Materials

Supplementary Materials

CsCl interface-driven structural resilience of $FAPbI_3$ to humidity

Gun-Hee Lee, Hui-Seon Kim*

Department of Chemistry and Chemical Engineering, Inha University, Incheon 22212, Republic of Korea.

***Correspondence to:** Prof. Hui-Seon Kim, Department of Chemistry and Chemical Engineering, Inha University, Incheon 22212, Republic of Korea. E-mail: hui-seon.kim@inha.ac.kr

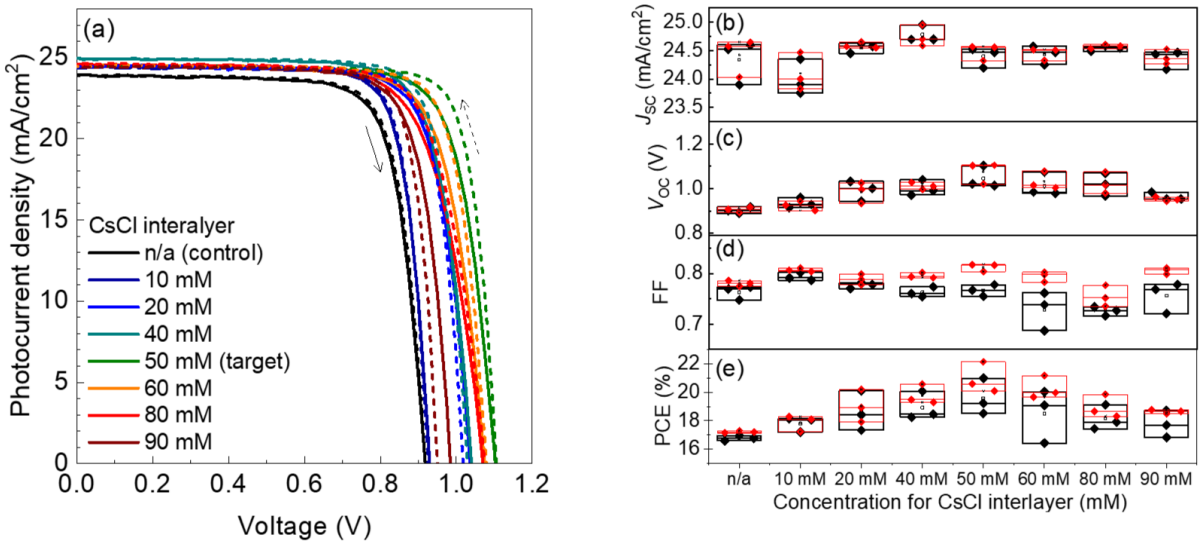

Figure S1 (a) Photocurrent density–voltage (J –V) curves of the champion devices as a function of the CsCl concentration. Statistical box plots of the photovoltaic parameters (b) J_{SC}, (c) V_{OC}, (d) fill factor (FF), and (e) PCE of PSCs with varying concentrations of CsCl. J–V curves and box plots of the photovoltaic parameters for devices with an active area of 0.16 cm^2. Black and red symbols in (b-e) denote the values obtained from forward and reverse scans, respectively.

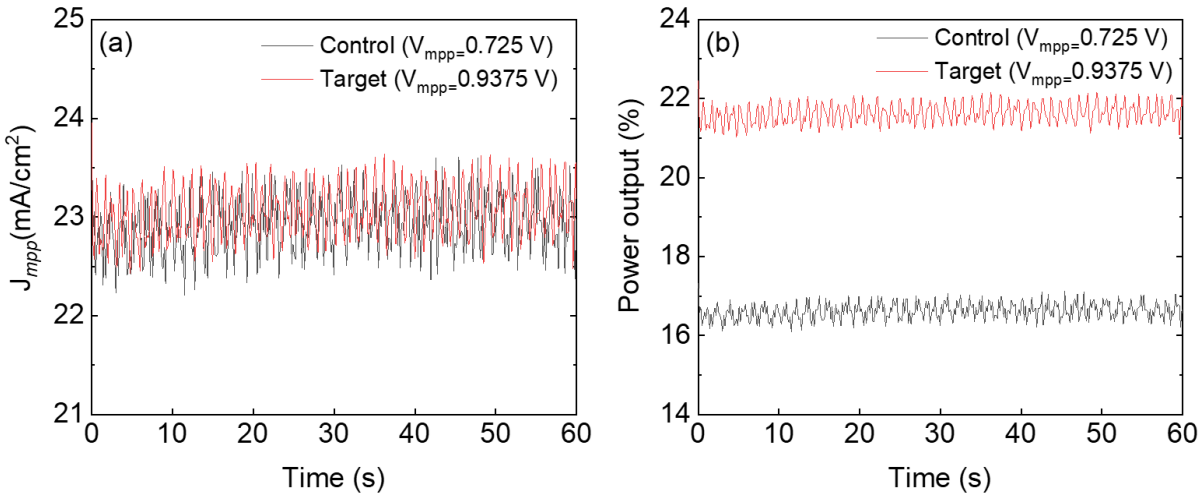

Figure S2 Time-dependent (a) photocurrent density and (b) power output of the control (black) and target (red) devices under mpp tracking.

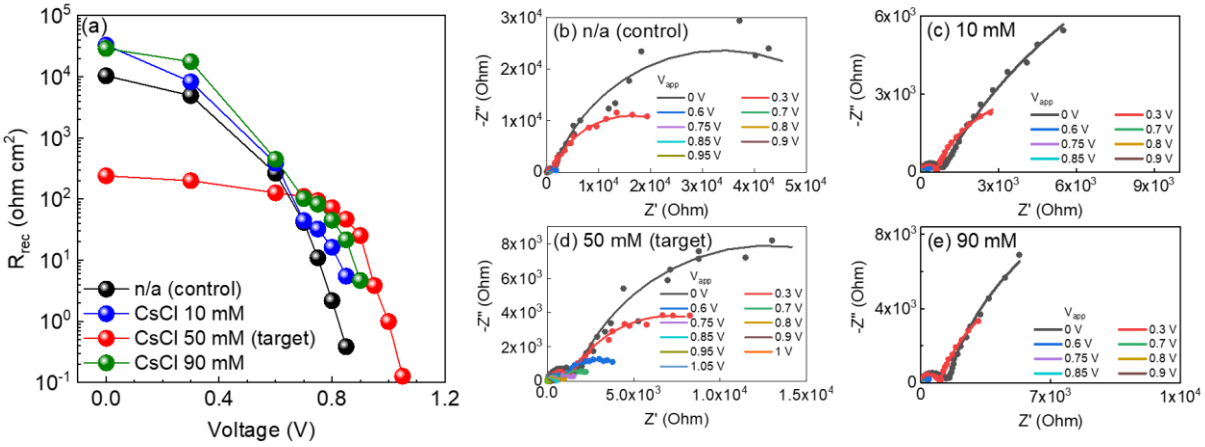

Figure S3 (a) R_{rec} as a function of applied voltage for devices with different CsCl interlayer concentrations. Black, blue, red, and green indicate the control device without a CsCl interlayer and the devices with CsCl interlayers prepared at 10 mM, 50 mM (target), and 90 mM, respectively. Nyquist plots (symbols) and fits (lines) for (b) the control device without a CsCl interlayer and the devices with CsCl interlayers prepared at (c) 10 mM, (d) 50 mM (target), and (e) 90 mM.

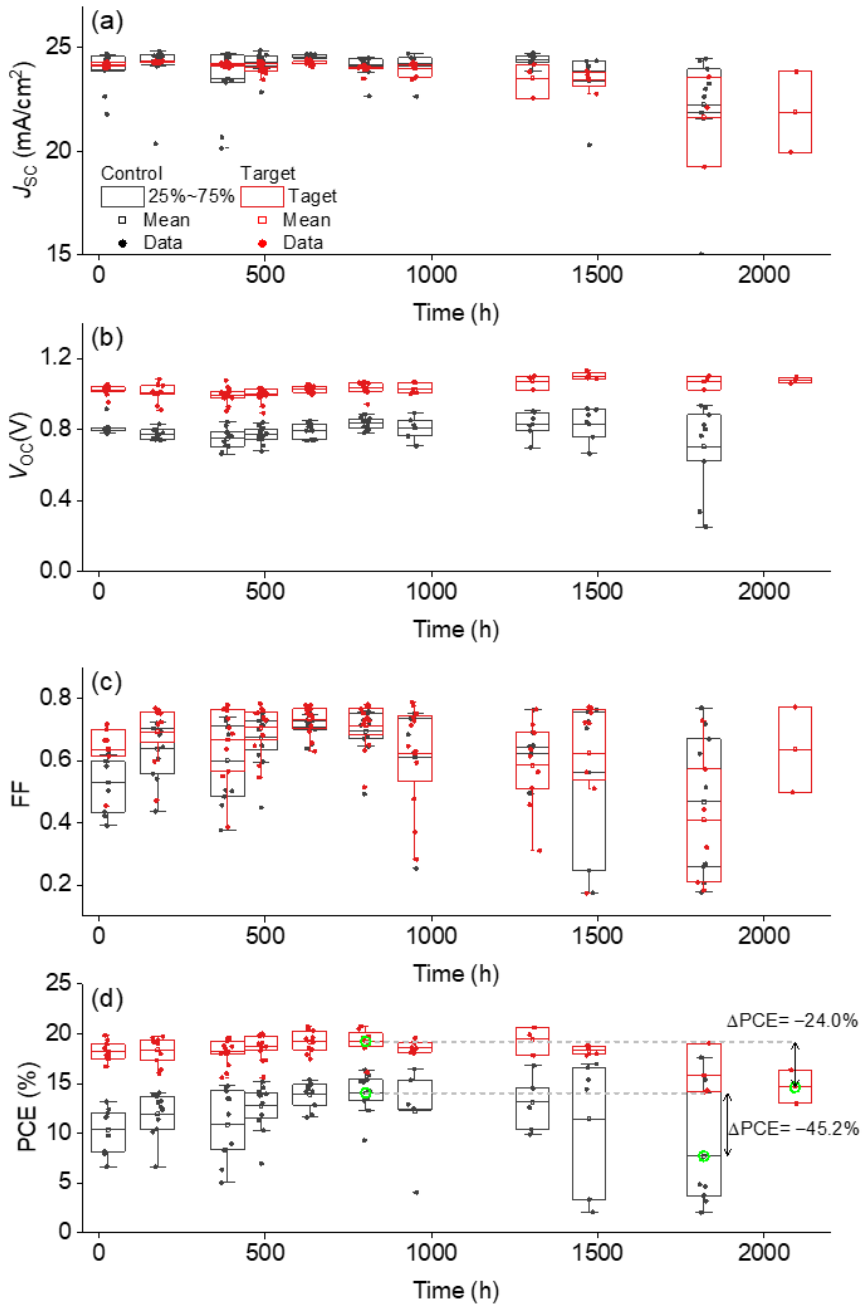

Figure S4 Statistical distribution of (a) J_{SC}, (b) V_{OC}, (c) FF, and (d) PCE of the control (black) and target (red) devices in the dark under ambient conditions. ΔPCE gives the relative change in mean PCE between the maximum value reached during storage and the final measurement, corresponding to −24.0% for the target devices and −45.2% for the control devices.

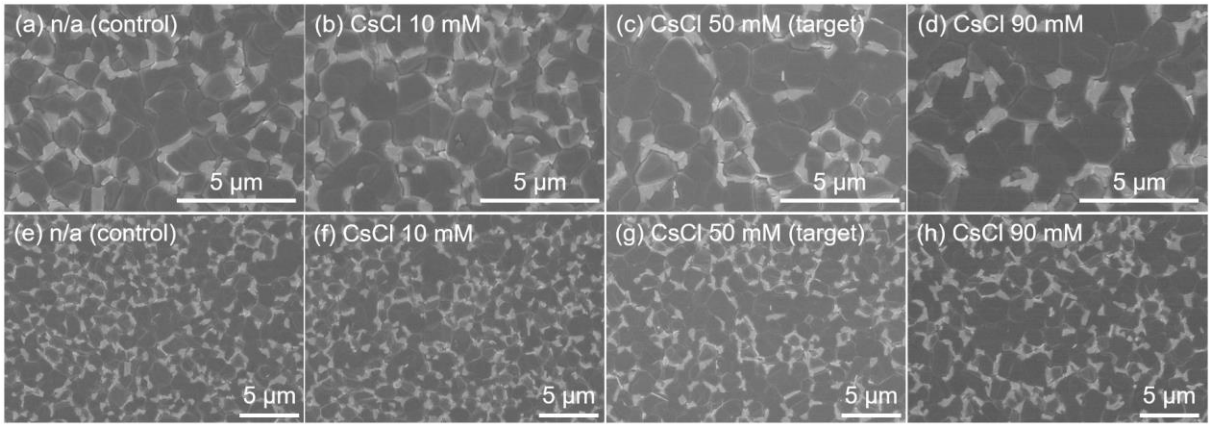

Figure S5 Surface SEM images of $FAPbI_3$ films deposited on CsCl-treated SnO_2 with varying the concentration of CsCl. (a, e) 0 mM (control), (b, f) 10 mM, (c, g) 50 mM (target), and (d, h) 90 mM. (a)–(d) are higher-magnification images, and panels (e)–(h) are lower-magnification views.

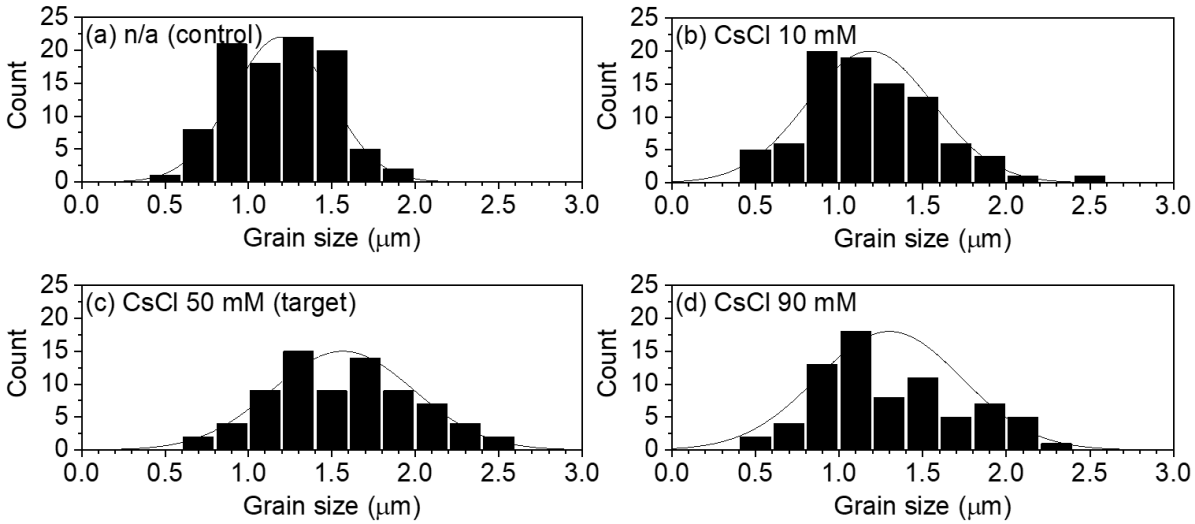

Figure S6 Grain-size distribution histograms of $FAPbI_3$ films deposited on CsCl-treated SnO_2 with varying the concentration of CsCl. (a) 0 mM (control), (b) 10 mM, (c) 50 mM (target), and (d) 90 mM.

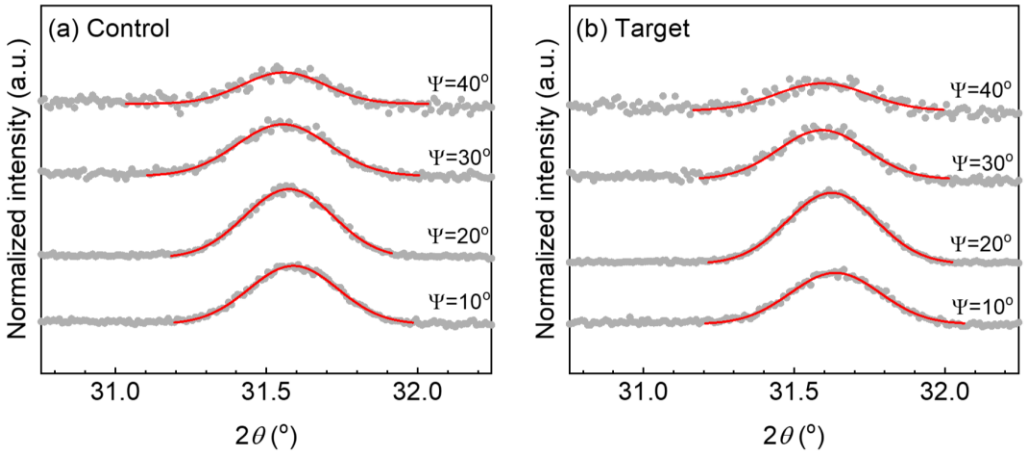

Figure S7 Normalized GIXRD patterns of the (a) control and (b) target films at tilt angles (Ψ) from 10° to 40°. Gray symbols and red lines represent the experimental data and the fitting results, respectively.

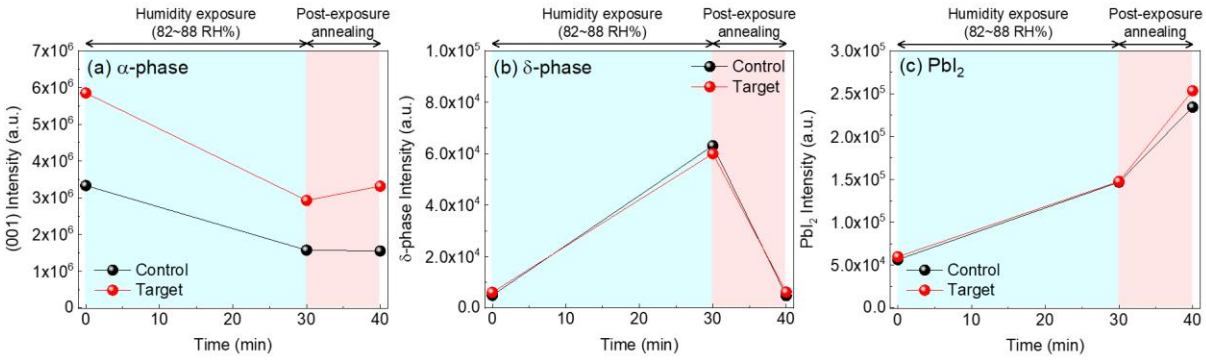

Figure S8 Evolution of XRD intensities of (a) α-phase, (b) δ-phase, and (c) PbI_2 for the control (black) and target (red) films at three stages: pristine at 0 min, humidity-exposed at 30 min (82–88% RH for 30 min), and post-exposure annealed at 40 min (170 ºC for 10 min).

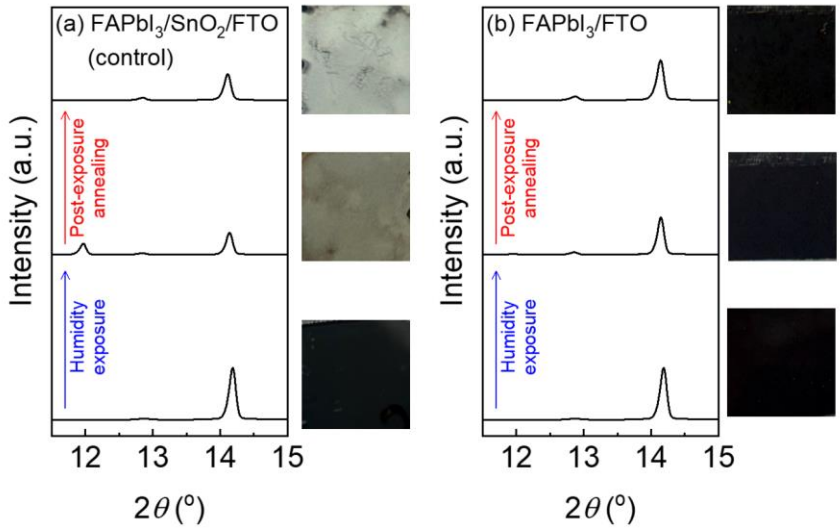

Figure S9 Evolution of XRD patterns for the $FAPbI_3$ films prepared on (a) SnO_2-deposited FTO substrate (control) and (b) bare FTO substrate, at three stages: pristine (bottom), humidity-exposed (middle), and post-exposure annealed (top). Humidity exposure was performed at 82–88% RH for 30 min, followed by post-exposure annealing at 170 °C for 10 min.

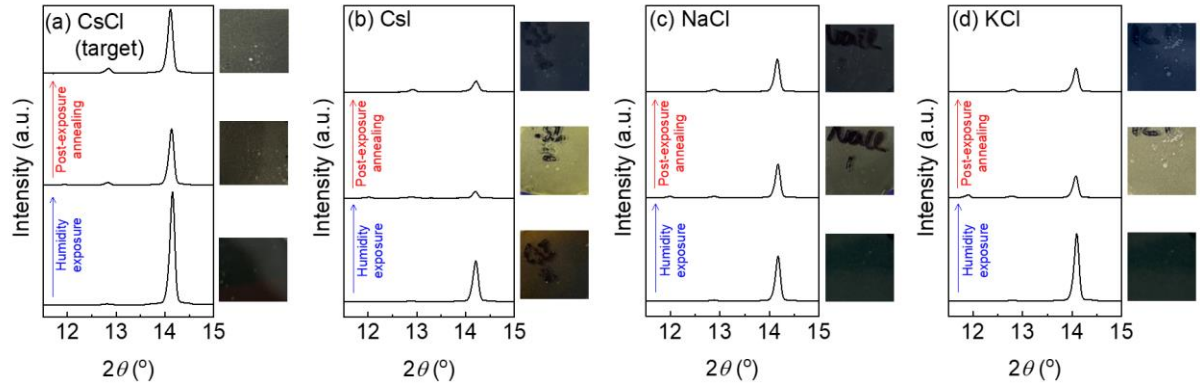

Figure S10 Evolution of XRD patterns for the $FAPbI_3$ films deposited on (a) CsCl (target), (b) CsI, (c) NaCl, and (d) KCl-treated SnO_2 substrates, at three stages: pristine (bottom), humidity-exposed (middle), and post-exposure annealed (top). Humidity exposure was performed at 82–88% RH for 30 min, followed by post-exposure annealing at 170 °C for 10 min.

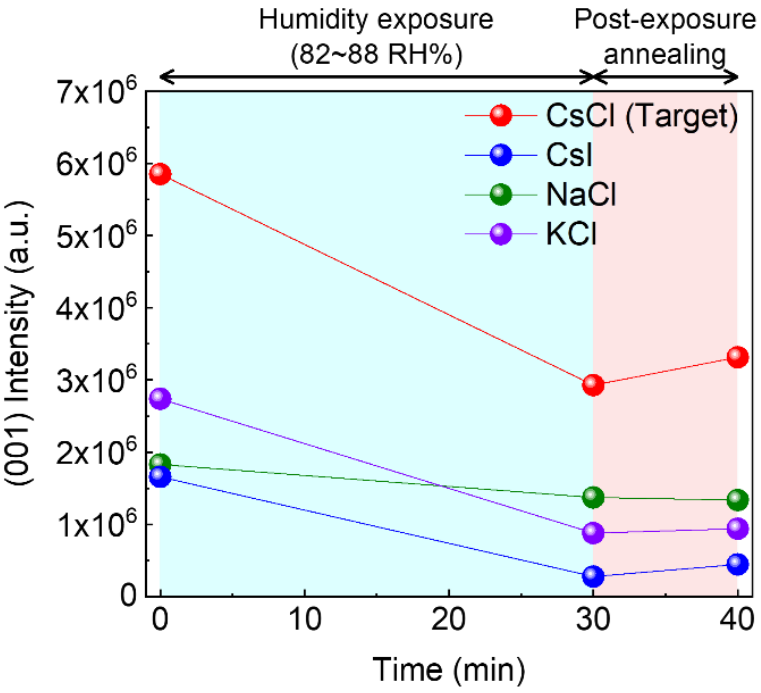

Figure S11 Evolution of (001) intensities of α-phase for the $FAPbI_3$ films deposited on CsCl (red, target), CsI (blue), NaCl (green), and KCl (purple)-treated SnO_2 substrates at three stages: pristine at 0 min, humidity-exposed at 30 min (82–88% RH for 30 min), and post-exposure annealed at 40 min (170 ºC for 10 min).

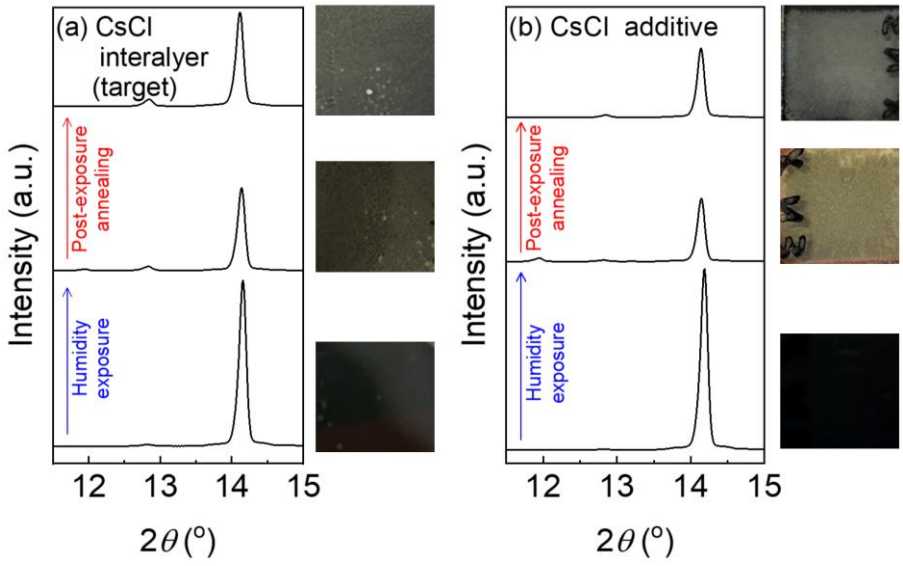

Figure S12 Evolution of XRD patterns for the $FAPbI_3$ films prepared with CsCl as (a) an interlayer (target) and (b) a precursor additive, at three stages: pristine (bottom), humidity-exposed (middle), and post-exposure annealed (top). Humidity exposure was performed at 82–88% RH for 30 min, followed by post-exposure annealing at 170 ºC for 10 min.

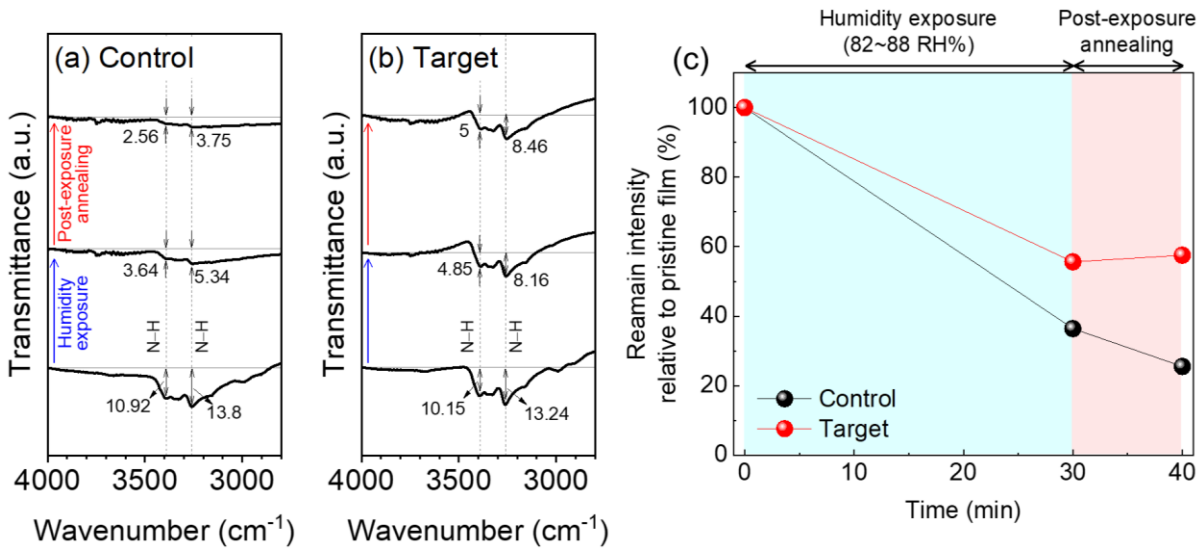

Figure S13 FT-IR spectra of the (a) control and (b) target films in the N–H stretching region, acquired at the pristine state (bottom), after humidity exposure (middle), and after post-exposure annealing (top). The numbers denote the intensities of the two N–H stretching bands located near 3400 and 3250 cm^{-1}, and the spectra are vertically offset for clarity. (c) Remaining N–H stretching intensity relative to that of the pristine film for the control and target films, plotted against the sequential humidity exposure (82–88% RH, 30 min) and post-exposure annealing (10 min) steps.

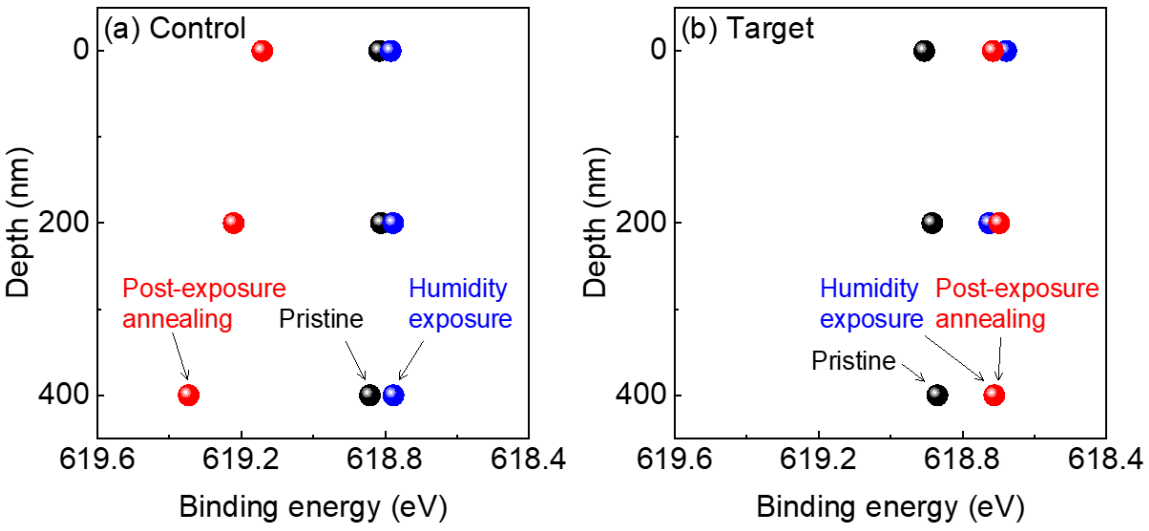

Figure S14 Depth-dependent I $3d_{5/2}$ XPS peak positions of the (a) control and (b) target films at the three sequential stages: pristine (black), humidity-exposed (blue), and post-exposure annealed (red).

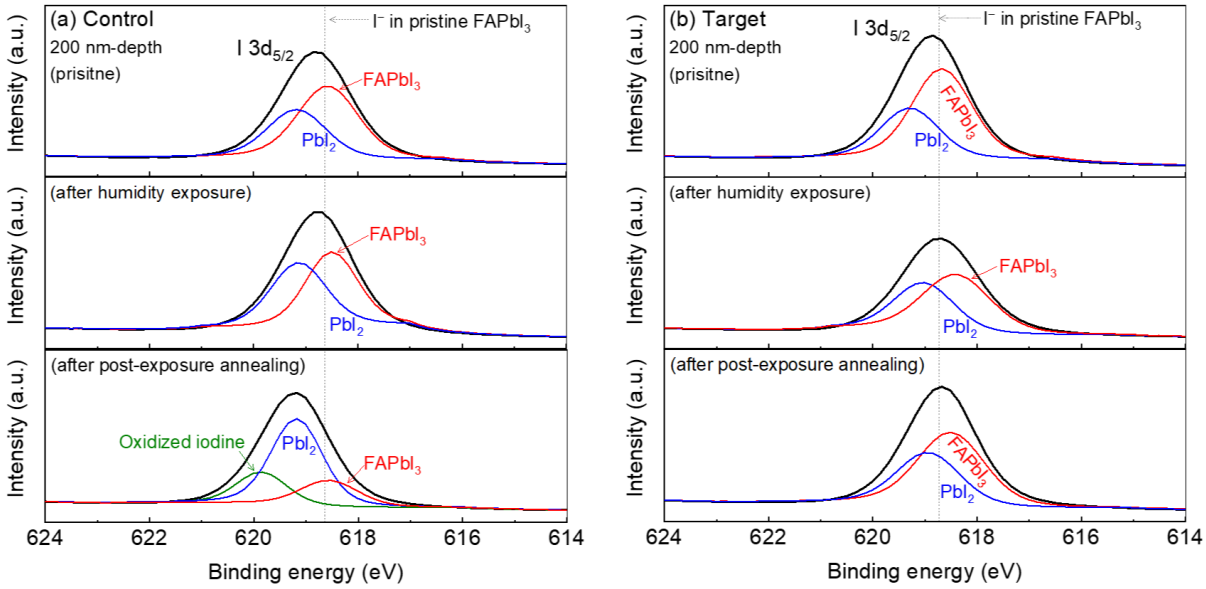

Figure S15 I $3d_{5/2}$ XPS spectra of the (a) control and (b) target films at the perovskite bulk (~200 nm depth), with dashed lines indicating I^- in the pristine $FAPbI_3$ lattice. Spectra were acquired at each of the three sequential stages.

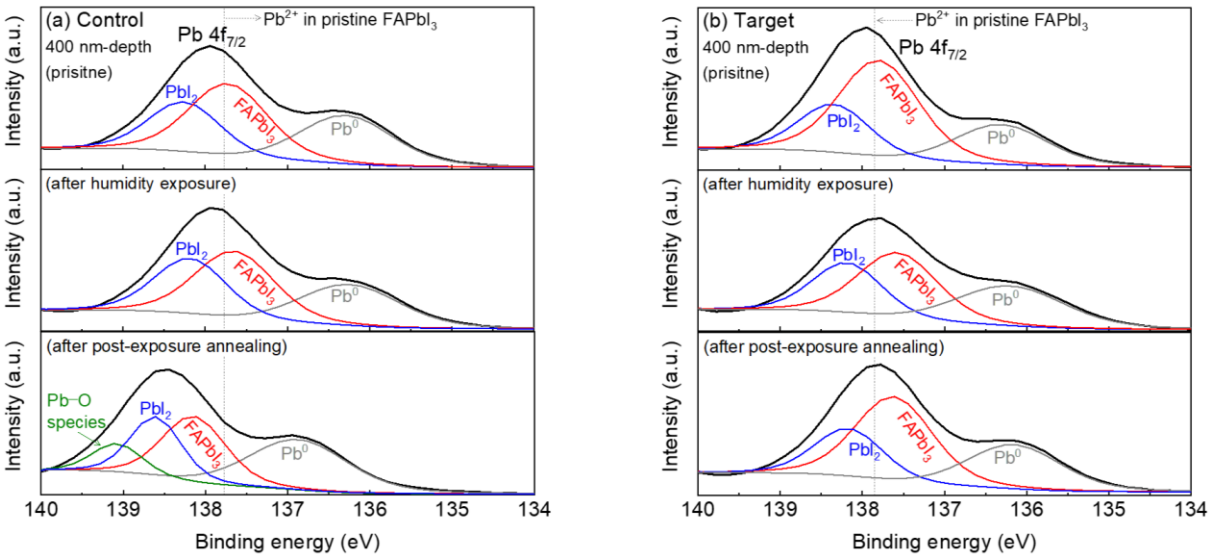

Figure S16 Pb $4f_{7/2}$ XPS spectra of the (a) control and (b) target films at a depth of ~400 nm, near the $SnO_2/FAPbI_3$ buried interface, with dashed lines indicating Pb^{2+} in the pristine $FAPbI_3$ lattice. Spectra were acquired at each of the three sequential stages.

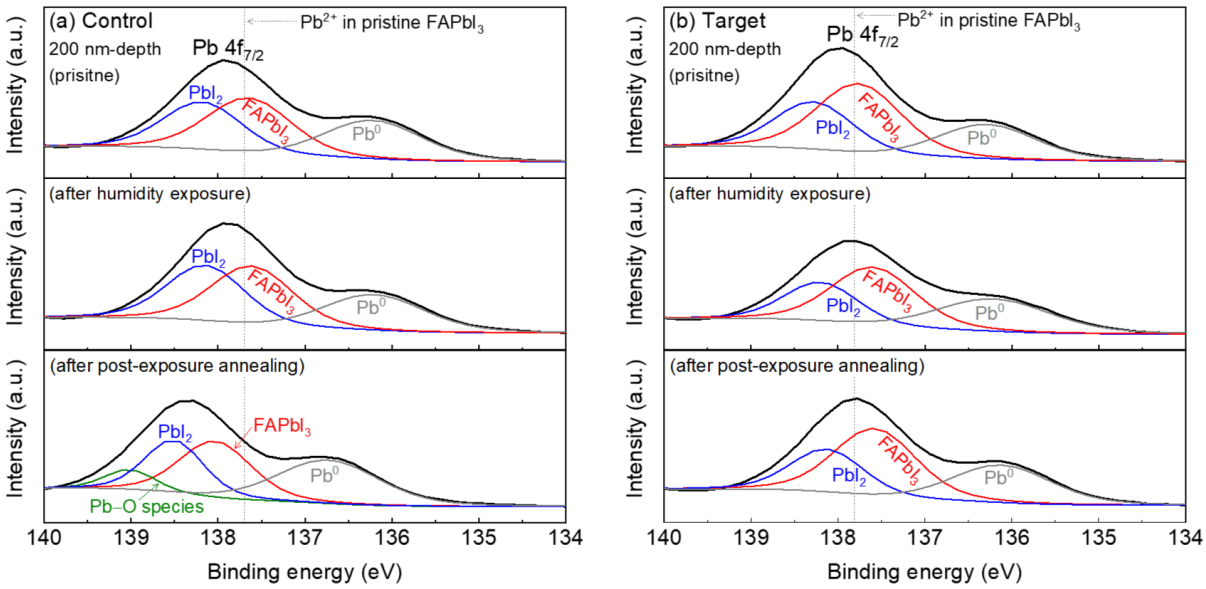

Figure S17 Pb $4f_{7/2}$ XPS spectra of the (a) control and (b) target films at the perovskite bulk (~200 nm depth), with dashed lines indicating Pb^{2+} in the pristine $FAPbI_3$ lattice. Spectra were acquired at each of the three sequential stages.

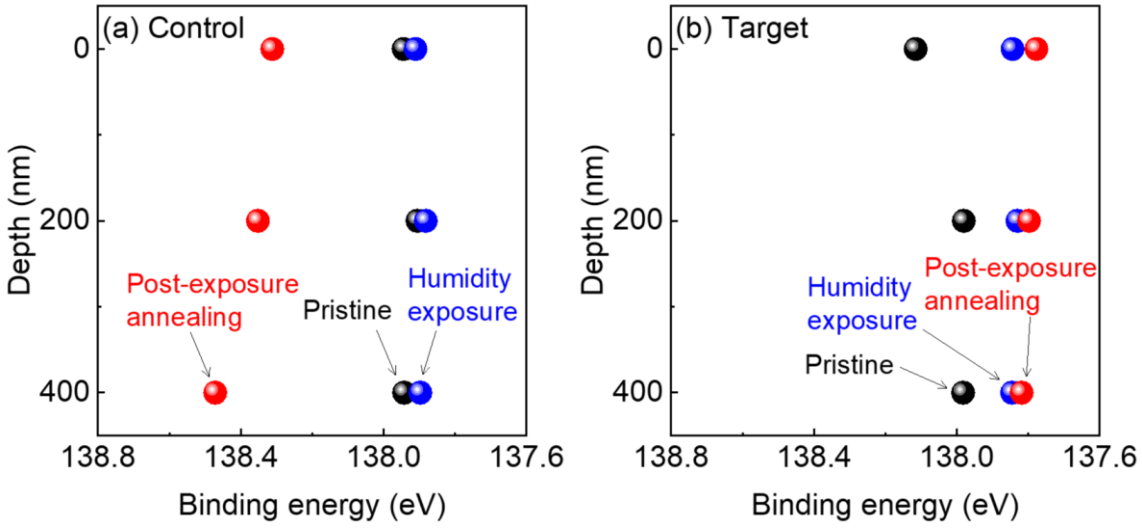

Figure S18 Depth-dependent Pb $4f_{7/2}$ XPS peak positions of the (a) control and (b) target films at the three sequential stages: pristine (black), humidity-exposed (blue), and post-exposure annealed (red).

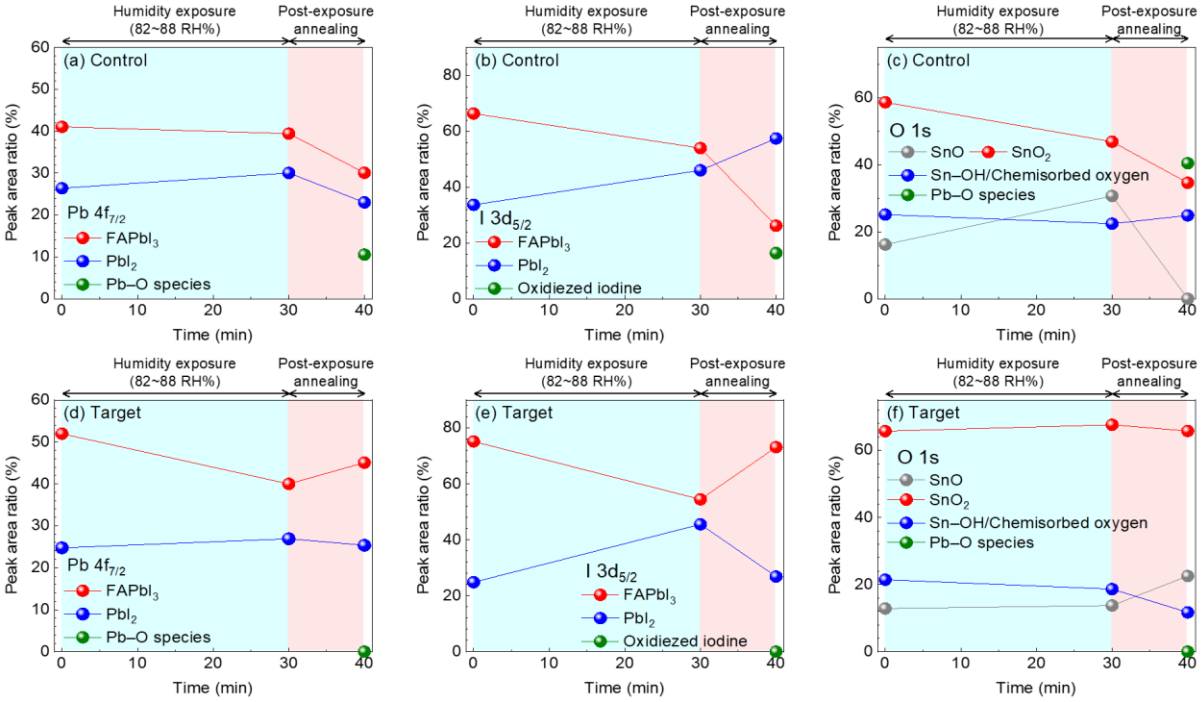

Figure S19 Peak area ratios obtained from the deconvoluted XPS spectra of the (a, d) Pb $4f_{7/2}$, (b, e) I $3d_{5/2}$, and (c, f) O 1s regions near the SnO_2/$FAPbI_3$ buried interface for the (a–c) control and (d–f) target films across the sequential stress steps: pristine (0 min), after humidity exposure at 82–88% RH (30 min), and after post-exposure annealing (40 min). The Pb $4f_{7/2}$ signal is resolved into $FAPbI_3$ (red), PbI_2 (blue), Pb^0 (not shown here) and Pb–O species (green). The I $3d_{5/2}$ signal into $FAPbI_3$ (red), PbI_2 (blue), and oxidized iodine (green). The O 1s signal into SnO_2 (red), SnO (grey), Sn–OH/chemisorbed oxygen (blue), and Pb–O-related species (green). The Pb $4f_{7/2}$ and I $3d_{5/2}$ XPS spectra were collected at a depth of 400 nm while the O 1s spectrum was collected at a depth of 600 nm, to capture the Pb and I signals from the perovskite and O signal from SnO_2 near the buried interface.

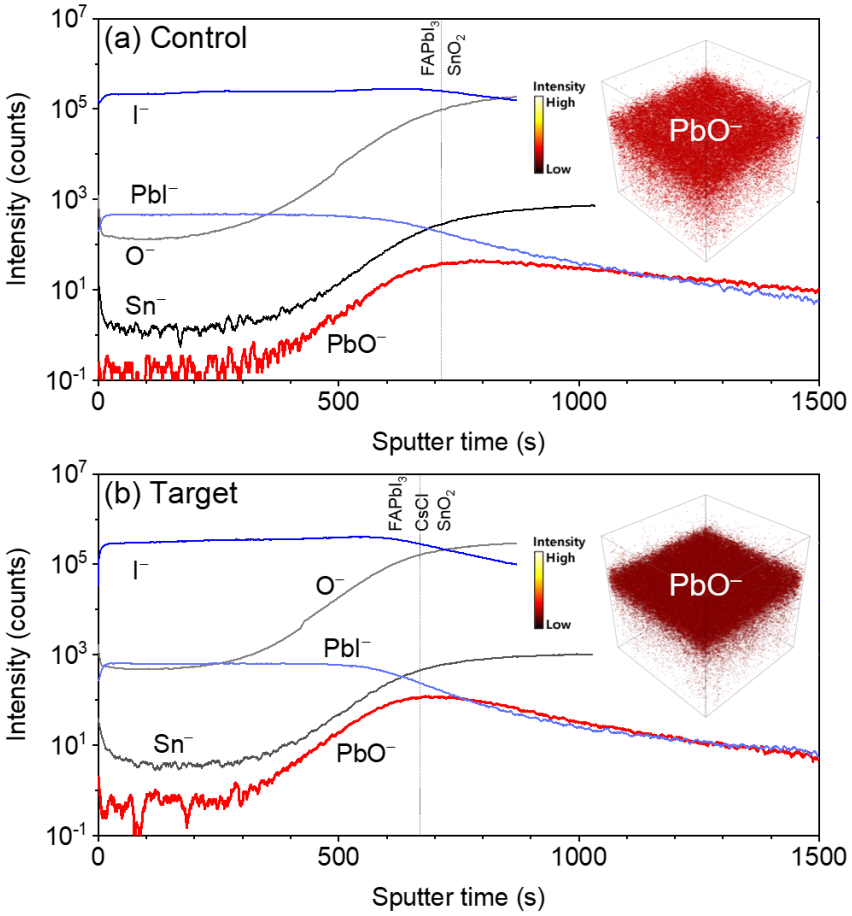

Figure S20 Negative-ion ToF-SIMS depth profiles of (a) control and (b) target films after post-exposure annealing, showing Sn^- (black), O^- (grey), I^- (blue), PbI^- (blue-violet), and PbO^- (red) signals as a function of sputtering time. Corresponding three-dimensional PbO^- ion maps of the control and target films are shown in the insets.